Patrimonio ambientale e transizione ecologica nei progetti di rigenerazione urbana e dei territori, Atti della XXV Conferenza nazionale SIU "Transizioni, giustizia spaziale e progetto

PASSIVE EFFECTS OF RARE-EARTH PERMANENT MAGNETS ON FLEXIBLE CONDUCTIVE STRUCTURES

Elvio Bonisoli, Alessandro Vigliani
Dipartimento di Meccanica, Politecnico di Torino

ABSTRACT

The paper presents a theoretical and experimental study of vibrating structures where paramagnetic or diamagnetic systems interact with rare-earth passive magnets.
The theoretical model of the system is focused on the damping properties of permanent magnets and on their interactions with the dynamic behaviour of an Euler-Bernoulli beam. In particular, the magnetic model is based on the analogy of the equivalent currents method in a quasi-static open-circuit-type configuration and it is used to determine the influence of eddy currents on the dynamic behaviour of conducting material structures. The magnetic effects are characterised by a viscous-type damping and by a stiffening dynamic effect of the structure, called "phantom effect".
The authors present the experimental outcomes for uniform cantilever clamped-free beams of different kinds of paramagnetic or diamagnetic conducting materials. It appears that the system frequency response can be modified by the presence of a pair of concordant or discordant permanent magnets of high residual induction settled at the free end.
Through the comparison between theoretical and experimental results, the paper demonstrates the validity of the model, that is able to describe both the above mentioned effect of dynamic stiffening of the structure and the considerable localised damping properties in paramagnetic or diamagnetic materials having low electric resistivity.

1. INTRODUCTION

The significantly enhanced properties of rare-earth permanent magnets, such as those sintered from Samarium-Cobalt or Neodymium-Iron-Boron, have permitted new interesting applications in mechanical field [1].
Both high coercive forces and hysteresis energy of these materials allow to obtain high non-linear magneto-elastic forces, such as those experienced in magnetic bearings, suspensions and levitation [2], and remarkable viscous-type damping properties, which are used to achieve high energy dissipation in magnetic dampers and eddy current brakes [3].

Furthermore rare-earth permanent magnets permit to increase the behaviour in reliability, thermal stability and proportionality as viscous damping elements, without mechanical friction [1]. They can also conveniently operate in vacuum; in particular, the considerable damping properties are here considered in mechanical couplings of dynamic systems in order to obtain localised dissipation of energy without mechanical contacts.

A vibrating uniform cantilever clamped-free beam of paramagnetic (aluminium) or diamagnetic (copper or brass) materials with low electric resistivity is considered, immersed in a quasi-static, spatially non constant, magnetic field produced by magnets fixed to the ground. In those material magneto-elastic forces are quite negligible and, hence, magneto-elastic buckling is not present [4, 5]. Experimental tests are conducted on this uniform cantilever clamped-free beam subject to the action of a pair of rare-earth permanent magnets, settled at the free end.

Experimentally, coupled with the high damping effect, a dynamic stiffening of the vibrating structure can also be observed, due to the magnetic interactions and called by the authors "phantom effect" [6].

An open-circuit-type magnetic model is proposed, built upon the analogy of the equivalent current method and developed from Laplace's inverse square law. It is suitable to describe both the observed dissipative and elastic magnetic effects and to consider the significant influence of boundary shape [7, 8]. Moreover, the authors propose a model suitable to correlate both effects to the eddy currents induced in the vibrating element. Thus, the dynamic stiffening effect, due to magneto-elastic repulsive force between permanent magnets and induced eddy currents, is modelled to be proportional to velocity.

In an equivalent single degree of freedom system a complex viscous-type damping coefficient is introduced, evaluated by the tri-dimensional magnetic model through energetic considerations and Ampere's force law [9].

Various concordant or discordant configurations of magnets are applied to an Euler-Bernoulli beam in bending vibrations; numerical results are then compared with experimental evidence. Finally, experimental transfer functions are compared to the analytical ones and the validity of the model is discussed.

2. MAGNETIC FIELD OF A PERMANENT MAGNET

A parallelepiped-rectangular shaped permanent magnet, sketched in Fig. 1, is considered. Based on the analogy of the equivalent current method, the magnet can be compared to a rectangular-coil solenoid; thus, referring to the Laplace's inverse square law, the infinitesimal contribution to the magnetic induction $d\mathbf{B}$ in a point $P(x,y,z)$ is [4, 9]:

$$d\mathbf{B} = \frac{\mu_0}{4\pi}\frac{i}{d^2}\frac{d\mathbf{s}\times\mathbf{u}_d}{}, \tag{1}$$

where d is the distance, identified by versor $\mathbf{u}_d$, from the infinitesimal portion $d\mathbf{s}$ set in $(u=0,v,w)$ of the side of a rectangular coil whose centre is in the reference system (x,y,z), $\mu_0 = 4\ \pi\ 10^{-7}$ H/m is the magnetic permeability of the vacuum and i is the current flowing through the coil; the vectorial product $d\mathbf{s}\times\mathbf{u}_d$, in the side of positive z parallel to y axis, results

$$d\mathbf{s}\times\mathbf{u}_d = \frac{-(z-c)\,dv}{\sqrt{x^2+(y-v)^2+(z-c)^2}}\,\mathbf{i} + \frac{x\,dv}{\sqrt{x^2+(y-v)^2+(z-c)^2}}\,\mathbf{k}, \tag{2}$$

where *a*, *b* and *c* are the magnet sizes.

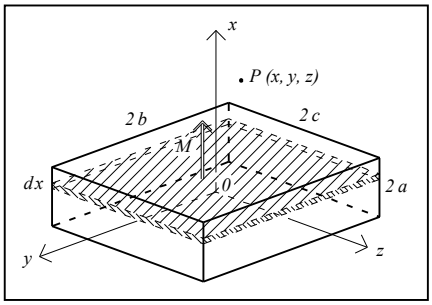

Fig. 1. Permanent magnet geometry

For the electro-mechanical analysis presented in the following sections, the contribution along the *x*-axis of magnetisation needs to be considered. Integrating along the four sides of the rectangular coil, the infinitesimal contribute to the magnetic induction dB_x is

$$\begin{aligned} dB_x = \frac{\mu_0\, i}{4\,\pi}\int_{-b}^{+b} \frac{(z+c)}{\left[x^2+(y-v)^2+(z+c)^2\right]^{3/2}} - \frac{(z-c)}{\left[x^2+(y-v)^2+(z-c)^2\right]^{3/2}}\,dv + \\ + \frac{\mu_0\, i}{4\,\pi}\int_{-c}^{+c} \frac{(y+b)}{\left[x^2+(y+b)^2+(z-w)^2\right]^{3/2}} - \frac{(y-b)}{\left[x^2+(y-b)^2+(z-w)^2\right]^{3/2}}\,dw \end{aligned} . \tag{3}$$

Let the residual magnetisation *M* be replaced with the linked currents *n i* per length unit of the equivalent solenoid; then, integrating along the length and assuming the relative permeability μ_r to be nearly unity, for the magnet sketched in Fig. 1, the value of the magnetic induction B_x can be expressed as:

$$B_x = \int_{-a}^{+a} dB_x(u) = \frac{\mu_0\, M}{4\,\pi}\int_{-a}^{+a} f_x(u)\; du, \tag{4}$$

where

$$\begin{aligned} f_x(u) = \frac{-(z+c)}{\left[(x-u)^2+(z+c)^2\right]}\cdot\left[\frac{(y-b)}{\left[(x-u)^2+(y-b)^2+(z+c)^2\right]^{1/2}} - \frac{(y+b)}{\left[(x-u)^2+(y+b)^2+(z+c)^2\right]^{1/2}}\right] + \\ + \frac{(z-c)}{\left[(x-u)^2+(z-c)^2\right]}\cdot\left[\frac{(y-b)}{\left[(x-u)^2+(y-b)^2+(z-c)^2\right]^{1/2}} - \frac{(y+b)}{\left[(x-u)^2+(y+b)^2+(z-c)^2\right]^{1/2}}\right] + \\ + \frac{-(y+b)}{\left[(x-u)^2+(y+b)^2\right]}\cdot\left[\frac{(z-c)}{\left[(x-u)^2+(y+b)^2+(z-c)^2\right]^{1/2}} - \frac{(z+c)}{\left[(x-u)^2+(y+b)^2+(z+c)^2\right]^{1/2}}\right] + \\ + \frac{(y-b)}{\left[(x-u)^2+(y-b)^2\right]}\cdot\left[\frac{(z-c)}{\left[(x-u)^2+(y-b)^2+(z-c)^2\right]^{1/2}} - \frac{(z+c)}{\left[(x-u)^2+(y-b)^2+(z+c)^2\right]^{1/2}}\right] \end{aligned} . \tag{5}$$

The gradient of the *x*-component of the magnetic induction is

$$\frac{dB_x}{dx} = -\frac{\mu_0\, M}{4\,\pi}\left[f_x(u=+a) - f_x(u=-a)\right], \tag{6}$$

i.e., the value of the variation of B_x over x evaluated in P equals the difference of the gradients of the magnetic induction originated by the two equivalent coils corresponding to the faces of the magnet.
It is worth noting that Eq. (6) predicts high variation of the distribution of the magnetic field in the surrounding space. Thus, in order to evaluate a characteristic value of the magnetic induction gradient, it is more rigorous to estimate a mean value on the surface linked with the magnetic flux and parallel to the face of the magnet, rather than to consider the axial value as an estimate for the whole surface. As shown in Fig. 2 and 3, both magnetic induction and its gradient are non-constant and present different distributions in any plane parallel to the terminal face of the magnet. With regard to the magnitude of the gradient, its maximum value shows the effect of demagnetisation, because of the presence of the magnetic poles.

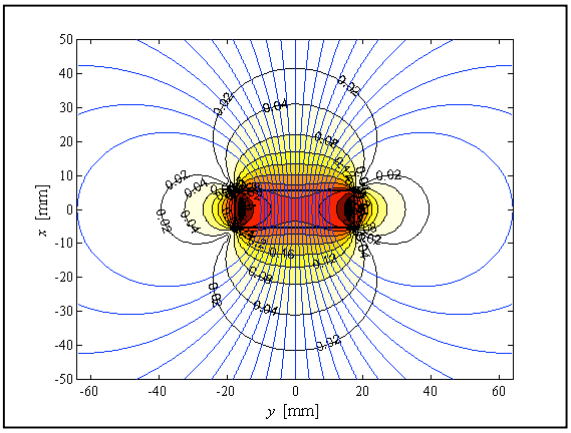

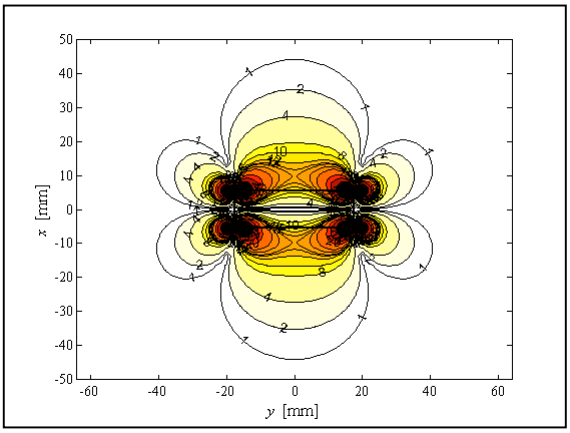

Fig. 2. and 3. Distributions of the magnetic induction (up) and of the corresponding gradient modulus (down)

The magnetic model is then used to evaluate the gradient of the magnetic induction generated on the symmetry plane $x = 0$ by two equal magnets disposed with opposite directions of magnetisation (Fig. 4). Because of the symmetry of the configuration, the magnetic induction on the considered plane is zero.
Variations of the air gap Δ between the two magnets significantly modify the distribution of the gradient of magnetic induction: therefore the mean value on the whole surface crossed by the magnetic flux is estimated.
Once the air gap is fixed, the constants for a model linearized in the neighbourhood of the origin can be obtained from Fig. 5. Through Taylor expansion, the mean gradient of the magnetic induction of the flux tube is given by

$$\frac{dB_{x,m}}{dx} = g(x_0) + g'(x_0)(x - x_0) + \frac{g''(x_o)}{2}(x - x_0)^2 + \ldots \cong \left.\frac{dB_{x,m}}{dx}\right|_{x=0}. \tag{7}$$

In the case a more realistic model is needed, a quadratic interpolation of the magnetic induction gradient can be chosen, by using both the mean and the axis values.
Considering permanent magnets with similar base sizes ($b \cong c$), the approximate distribution of the gradient takes the form:

$$\frac{dB_x}{dx}(x,y) = \frac{dB_{x,a}}{dx} + \left(\frac{\dfrac{dB_{x,m}}{dx} - \dfrac{dB_{x,a}}{dx}}{\bar{\xi}^2} \right) y^2, \quad \text{where} \quad \bar{\xi} = \frac{3}{4}\frac{(b+c)}{2}. \tag{8}$$

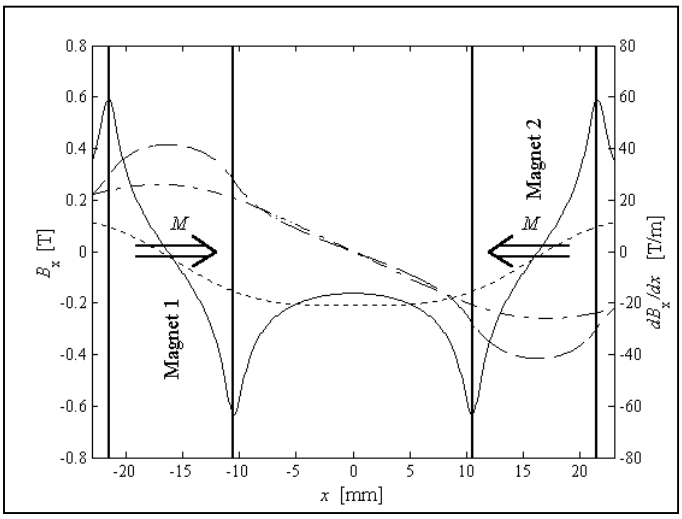

Fig. 4. Distributions of magnetic induction and of its gradient for two repulsive permanent magnets with an air gap Δ = 21 mm: magnetic induction on the axis $B_{x,a}$ (–·) and mean value of the flux tube $B_{x,m}$ (--), magnetic induction gradient on the axis $d\,B_{x,a}/d\,x$ (··) and mean value of the flux tube $d\,B_{x,m}/d\,x$ (–)

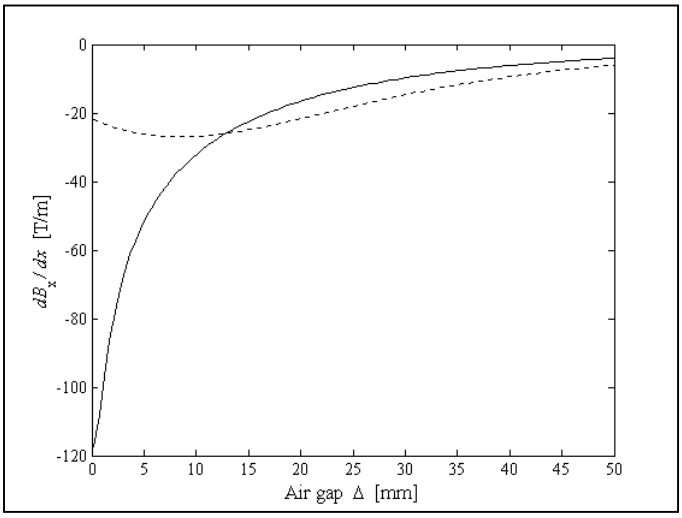

Fig. 5. Magnetic induction gradient on the axis (··) and mean value of the flux tube (–)

In the magnetic pattern shown in Fig. 4, through the expression of the magnetic force magnitude per unit volume $F_v = M\,dB_x/dx$ [4, 9], the repulsive force between the two permanent magnets may be estimated.

For rare-earth materials the hysteresis loop is nearly square in shape so that the magnetisation *M* is likely to be constant for values of the demagnetising field lower than the coercive force intensity [7]. A consequence of the rigidity of the magnetisation is that the superposition of

flux produced by rare-earth permanent magnets is linear, and the magnetic material is effectively transparent, behaving like vacuum.
Therefore, for a pair of similar magnets in attraction or repulsion, the magnetisation *M* of each magnet is not influenced by the magnetic field generated by the other one. In addition, for rare-earth magnets, the magnetisation *M* can be reasonably considered unidirectional and of constant magnitude throughout the volume of the magnet.
Thus, assuming a relative permeability μ_r = 1, the repulsive magnetic force applied by the first magnet on the second one is given by:

$$F_{1,2} = \frac{B_{r,1}}{\mu_0} \int_{-c}^{+c} \int_{-b}^{+b} \int_{a+\Delta}^{3a+\Delta} \frac{dB_{x,2}}{dx}\, dx\, dy\, dz = \frac{B_{r,1}}{\mu_0}\, 4\,b\,c\, \left[B_{x,m,2}\left(x = 3a + \Delta\right) - B_{x,m,2}\left(x = a + \Delta\right) \right], \qquad (9)$$

where Δ is the air gap between the two magnets and $B_{x,m}$ is the mean magnetic induction evaluated on the terminal faces of the second magnet.

For experimental comparison, the authors used permanent magnets on a sintered base of Samarium and Cobalt, having dimensions *2a* = 11 mm, *2b* = 35 mm, *2c* = 30 mm and residual magnetic induction $B_r = \mu_0 M$ = 1.0 T. To test the validity of the magnetic model, the repulsive magnetic forces are experimentally measured by varying a static load on the upper magnet, free to move only vertically and, consequently, by varying the air gap Δ. The experimental results are compared with the model predictions (Eq. 9) in Fig. 6, which shows a very good agreement between the data.
In order to further validate the magnetic model, the magnetic induction was directly measured on different planes parallel to the magnet face by means of a Hall effect transducer. As shown in Fig. 7, in general a good agreement between the magnetic model and the experimental results is observed, with less than 8% relative errors. In particular, it is worth noting that experimental values result from a mean of the 6 mm^2 surface covered by the Hall transducer; thus, the boundary effects predicted by the model and shown in Fig. 2 and 3 are substantially verified, although affected by errors in proximity of high variable magnetic induction distributions.

Therefore, in magnetostatic problems the analogy of the equivalent currents for the permanent magnets used in the model represent a valid and useful approach to predict the magnetic induction, its gradient and magneto-elastic forces, because it requires only the knowledge of the assigned geometry and the residual magnetic induction of the permanent magnets.

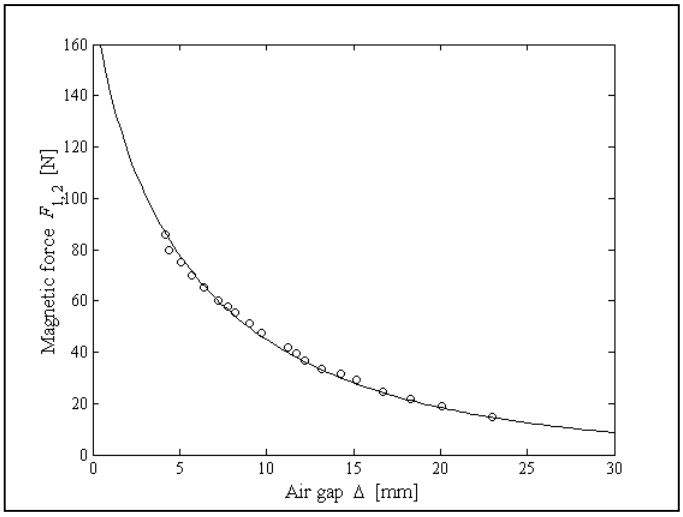

Fig. 6. Experimental comparison of the magneto-elastic repulsive force:
(–) analytical magneto-elastic force, (o) experimental values

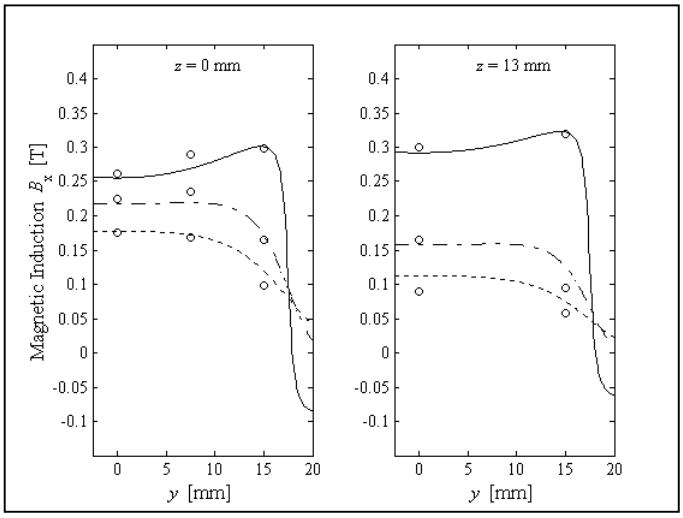

Fig. 7. Experimental comparison of the magnetic induction:
analytical magnetic induction in plane x = 6 mm (–), x = 9 mm (–·), x = 12 mm (··), (o) experimental values

3. MAGNETIC EFFECTS ON A SDOF DYNAMIC SYSTEM

A single degree of freedom (sdof) system of mass m, stiffness k and damping coefficient c_v as shown in Fig. 8 is considered. A pair of equal permanent magnets, with opposite magnetisation, are located on both sides of the conducting mass, characterised by resistively r and having dimensions h, $2b$, $2c$, with an air gap Δ (Moon-Holmes pattern [10]).

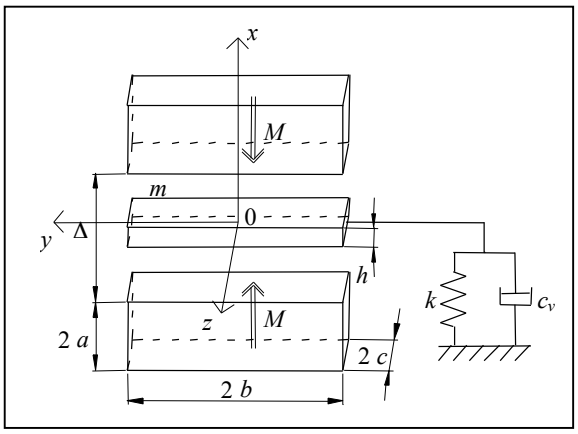

Fig. 8. Single degree of freedom dynamic system

The influence of the two magnets as damping elements is here analysed. The well-known equation of motion of the system is:

$$m\,\ddot{x} + \left(c_v + c_m\right)\dot{x} + k\,x = 0, \tag{10}$$

where c_m is the coefficient of the magnetic viscous damping produced by the Joule effect due to the flow of an induced current [3, 11].

The coefficient c_m can be obtained by expressing the dissipated power P_d as

$$P_d = F_m\,\dot{x}^2 = c_m\,\dot{x}^2 = \frac{fem^2}{R} = R\,i^2, \tag{11}$$

where F_m is the viscous force, i is the induced current, R is the electrical resistance of the conducting mass and *fem* is the electromotive force evaluated through Faraday's electromagnetic induction law

$$fem = -\,\dot{x}\int_s \frac{dB_x}{dx}\,ds\,. \tag{12}$$

In Eq. (12) dB_x/dx represents the gradient of magnetic induction estimated using the previous magnetic model linearized in the neighbourhood of the undeformed configuration of the system (x = 0 mm).

Eddy currents arise in opposition to the gradient of magnetic field inside the mass, which can be therefore considered as a coil where currents flow to generate a magnetic induction opposed to the gradient produced by the two magnets.

Assuming a constant gradient of the magnetic induction on the whole surface, the electromotive force can be considered approximately proportional to the integrating domain, i.e. to the square of the distance from the x-axis. Furthermore, under the hypothesis that currents run into rectangular concentrical circuits, currents appear to undergo linear variation with the distance from the x-axis.

Consequently, using permanent magnets with similar base size ($b \cong c$), the electromotive force is:

$$fem\left(y\right) = -\,\dot{x}\,\frac{2b\;2c}{b^2}\,y^2\,\frac{dB_{x,m}}{dx}, \tag{13}$$

with $y \in [0\,,\,b]$, while the resistance of a ring of infinitesimal section $h\,dy$ is

$$dR\left(y\right) = r\,\frac{4\,\dfrac{b+c}{b}\,y}{h\,dy}. \tag{14}$$

Therefore, the global current i flowing through the vibrating element is

$$i = \int_0^{i_{\max}} d\,i\left(y\right) = \int_0^b -\,\dot{x}\,\frac{c\;h}{r\left(b+c\right)}\,\frac{dB_{x,m}}{dx}\,y\,dy = -\,\dot{x}\,\frac{b^2\,c\;h}{2\,r\left(b+c\right)}\,\frac{dB_{x,m}}{dx}. \tag{15}$$

Using Eq. (13) and knowing current i from (15), the global electrical resistance R is

$$R = r\,\frac{4\left(b+c\right)}{b\;h} \cong r\,\frac{8}{h}. \tag{16}$$

Hence, the power P_d dissipated by Joule effect is proportional to the square of the velocity of vibrating element, i.e.:

$$P_d = c_m \dot{x}^2 = \dot{x}^2 \frac{b^3 c^2 h}{r (b+c)} \left(\frac{dB_{x,m}}{dx} \right)^2 ; \tag{17}$$

finally, the magnetic viscous damping coefficient c_m can be expressed as:

$$c_m = \frac{b^2 c^2 h}{2 r} \left(\frac{dB_{x,m}}{dx} \right)^2 . \tag{18}$$

The flow of relevant induced currents inside the conductor generates a variable magnetic field that produces a magneto-elastic force. This essentially dynamic phenomenon, called "phantom effect", affects the response of the mass. If the mass is excited by a harmonic force $F = F_0 \, \mathrm{e}^{\mathrm{j}\,\omega\, t}$ with $\omega > 0$, the equation of motion of the system (Eq. 10) becomes:

$$m \ddot{x} + \left(c + c_m - \mathrm{j}\, c_e \right) \dot{x} + k\, x = F_0 \, \mathrm{e}^{\mathrm{j}\,\omega\, t} , \tag{19}$$

where c_e is the coefficient corresponding to the phantom effect, and j is the imaginary operator, introduced because the associated elastic force $F_e = - c_e \dot{x}$ is conservative and therefore, even though proportional to the velocity, it is in phase with the displacement of the mass.
In fact, the induced eddy currents tend to bring the conducting element back to the undeformed configuration, which basically indicates that the system stiffness has increased.

The term "phantom effect" is chosen to underline its hidden dynamic nature. In fact, the effect of eddy currents, corresponding to a conservative force, is not immediately visible because it does not affect the system damping properties; nevertheless, its importance cannot be neglected, like experiments reveal, especially in systems with high natural frequency. In fact, the effect of the magnetic force causes a shift towards the right of the system natural frequencies, proportional to the natural frequency, which contrasts the reduction of the natural frequencies caused by viscous damping.
To the author's knowledge this phenomenon, that has never described and modelled before, is particularly interesting: it appears to be analogous to the well known hysteretic structural damping, used to describe the dynamic dissipative behaviour of structural and viscoelastic materials [12, 13]. In the present work the authors used the same definition to represent a conservative term dependent on velocity.

The coefficient c_e can be derived from the equation relating the elastic force F_e to the electromechanical interaction between currents and magnetic field. Analogously to Eq. (9), such a relation can be obtained by integrating the magnetic force magnitude per unit volume over the volume of the conductor:

$$F_e = - c_e \dot{x} = \int_v n\, i \frac{dB_x}{dx} \, dv . \tag{20}$$

Due to the symmetry gradient of magnetic induction, not all the circulating eddy currents into the element produce a concordant resultant elastic force F_e; thus it is necessary to introduce a

volume coefficient $\chi \in [0.25\ ,\ 1]$, whose value may be estimated by means of experimental outcomes.
The magneto-elastic force becomes

$$F_e = -\,c_e\ \dot{x} = \chi \int_0^{i_{\max}} \frac{dB_{x,m}}{dx}\ \frac{2b\ 2c}{b^2}\ y^2\ di(y) = -\,\dot{x}\ \chi\ \frac{b^3\ c^2\ h}{r\ (b+c)} \left(\frac{dB_{x,m}}{dx}\right)^2, \tag{21}$$

while for the magnetic stiffening coefficient c_e it holds:

$$c_e = \chi\ \frac{b^2\ c^2\ h}{2\ r} \left(\frac{dB_{x,m}}{dx}\right)^2. \tag{22}$$

It results that both c_m and c_e grow with the square of the variation of the mean magnetic induction through the element, they depend on the geometry of the element and they are inversely proportional to the resistivity *r* of the material.
It is worth noting that both effects depend on the same cause, i.e. the induced currents, that do not appear in the dynamic equilibrium Eq. (19). Obviously, since their value depends on the velocity $\dot{x}$, a mathematical solution would hold also if only one of two effects (the damping coefficient) was taken into account, but experimental evidence, i.e. the increase of the system stiffness, cannot be explained by a viscous term alone.

Under the hypothesis of a constant distribution of the magnetic induction gradient, the two magnetic coefficient are related by the simple linear relation $c_e = \chi\ c_m$, while if the quadratic interpolation of Eq. (8) is used, values of c_m and c_e can be determined more precisely. Under this assumption, the electromotive force becomes:

$$fem\ (y) = -\,\dot{x}\ \frac{4\ c}{b}\ y^2 \left[\frac{dB_{x,a}}{dx} + \left(\frac{\dfrac{dB_{x,m}}{dx} - \dfrac{dB_{x,a}}{dx}}{\bar{\xi}^2}\right) \frac{y^2}{2}\right], \tag{23}$$

with $y \in [0\ ,\ b]$. Hence current *i*, flowing through the vibrating element, can be expressed as

$$i = -\,\dot{x}\ \frac{b^2\ c\ h}{2\ r\ (b+c)} \left[\frac{dB_{x,a}}{dx} + \left(\frac{\dfrac{dB_{x,m}}{dx} - \dfrac{dB_{x,a}}{dx}}{\bar{\xi}^2}\right) \frac{b^2}{4}\right], \tag{24}$$

while the dissipated power produced by Joule effect is

$$P_d = c_m\ \dot{x}^2 = \dot{x}^2\ \frac{b^3\ c^2\ h}{r\ (b+c)} \left[\left(\frac{dB_{x,a}}{dx}\right)^2 + \frac{dB_{x,a}}{dx}\ \frac{\dfrac{dB_{x,m}}{dx} - \dfrac{dB_{x,a}}{dx}}{\bar{\xi}^2}\ \frac{2b^2}{3} + \frac{\left(\dfrac{dB_{x,m}}{dx} - \dfrac{dB_{x,a}}{dx}\right)^2}{\bar{\xi}^4}\ \frac{b^4}{8}\right] \tag{25}$$

The magnetic viscous damping coefficient c_m can now be evaluated; it yields:

$$c_m = \frac{b^2\ c^2\ h}{2\ r}\left[\left(\frac{dB_{x,a}}{dx}\right)^2 + \frac{dB_{x,a}}{dx}\ \frac{\frac{dB_{x,m}}{dx} - \frac{dB_{x,a}}{dx}}{\bar{\xi}^2}\ \frac{2b^2}{3} + \frac{\left(\frac{dB_{x,m}}{dx} - \frac{dB_{x,a}}{dx}\right)^2}{\bar{\xi}^4}\ \frac{b^4}{8}\right]. \tag{26}$$

Using Eqs. (8) and (24), the magneto-elastic force, proportional to velocity, becomes:

$$F_e = -\ \dot{x}\ \chi\ \frac{b^3\ c^2\ h}{r\ (b+c)}\left[\left(\frac{dB_{x,a}}{dx}\right)^2 + \frac{dB_{x,a}}{dx}\ \frac{\frac{dB_{x,m}}{dx} - \frac{dB_{x,a}}{dx}}{\bar{\xi}^2}\ b^2 + \frac{\left(\frac{dB_{x,m}}{dx} - \frac{dB_{x,a}}{dx}\right)^2}{\bar{\xi}^4}\ \frac{b^4}{4}\right]; \tag{27}$$

hence the magnetic stiffening coefficient c_e is:

$$c_e = \chi\ \frac{b^2\ c^2\ h}{2\ r}\left[\left(\frac{dB_{x,a}}{dx}\right)^2 + \frac{dB_{x,a}}{dx}\ \frac{\frac{dB_{x,m}}{dx} - \frac{dB_{x,a}}{dx}}{\bar{\xi}^2}\ b^2 + \frac{\left(\frac{dB_{x,m}}{dx} - \frac{dB_{x,a}}{dx}\right)^2}{\bar{\xi}^4}\ \frac{b^4}{4}\right]. \tag{28}$$

Of course, if the hypothesis of a constant distribution of the magnetic induction gradient does not hold, the linear relation between c_m and c_e is lost.

As shown in Fig. 9, for the considered permanent magnets and a 3 mm thick aluminium mass (r_{Al} = 2.65 10^{-8} Ω m), if an air gap Δ = 21 mm is set and χ = 0.25 is assumed, a constant distribution of the magnetic induction gradient through Eqs. (18) and (22) gives c_m = 0.9458 Ns/m and c_e = 0.2364 Ns/m, whereas from the quadratic interpolation of Eqs. (26) and (28) it yields c_m = 1.1659 Ns/m and c_e = 0.2315 Ns/m (cfr. Table 1).

In the range of air gap 5-30 mm, the maximum relative error between the two distribution hypotheses is approximately ± 30% in determining c_m and ± 4% when estimating c_e. Obviously the minimum relative error is reached when the mean magnetic induction gradient is equal to the axial value; experimental evidence proves that a more realistic solution can be achieved by means of Eqs. (26) and (28).

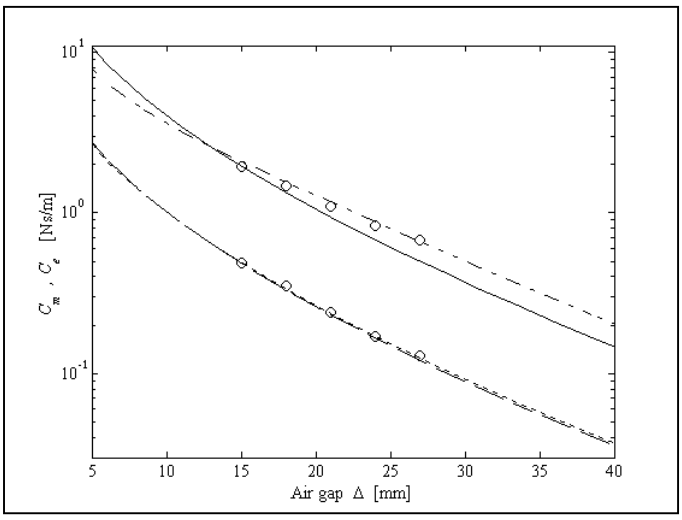

Fig. 9. Experimental comparison of the damping coefficients: (–) c_m and (··) c_e with constant distribution of the magnetic induction gradient, (–·) c_m and (--) c_e with quadratic interpolation of the magnetic induction gradient distribution, (o) experimental values

Eq. 19 can be written in non-dimensional form as

$$\ddot{x} + 2\xi_m \frac{1 + \mathrm{j}\psi}{\sqrt{1+\psi^2}} \omega_n \dot{x} + \omega_n^2 x = \frac{F_0}{k} \omega_n^2 \mathrm{e}^{\mathrm{j}\omega t}, \tag{29}$$

where $\omega > 0$ and

$$\xi_m = \frac{\sqrt{(c_v + c_m)^2 + c_e^2}}{2\sqrt{k\,m}}, \quad \psi = \frac{-c_e}{c_v + c_m} \quad \text{and} \quad \omega_n = \sqrt{\frac{k}{m}}; \tag{30}$$

hence, for the dynamic system represented in Fig. 8, the well-known expression of the frequency response function results

$$H_n(\omega) = \frac{X_0}{\left(\frac{F_0}{k}\right)} = \frac{1}{1 + \mathrm{j}2\xi_m \frac{1+\mathrm{j}\psi}{\sqrt{1+\psi^2}} \frac{\omega}{\omega_n} - \left(\frac{\omega}{\omega_n}\right)^2}. \tag{31}$$

The influence of the complex viscous damping coefficient of Eq. (29) can be evaluated by means of a geometrical representation in the Argand-Gauss plane involving rotating vectors: the damping force vector is no longer orthogonal to the stiffness force vector, so that the projection of the first on the second represents a stiffness increase, proportional to velocity. Though it has not been experimentally verified for magnetic configuration, this model allows to describe, without loss of generality, also a stiffening decrease proportional to velocity when $\psi > 0$, corresponding to an inertial increase. Thus it is underlined the flexibility of the model.

The behaviour of both modulus and phase of the frequency response function (Bode plots) depends on the parameters ξ_m and ψ, as shown in Fig. 10 and 11 (for $\psi = -0.75$). Note that for increasing values of ξ_m, the resonance peaks (represented with • in Fig. 10) shift towards higher values of frequency, showing an opposite behaviour with respect to the case of real viscous damping models. Moreover, as ξ_m approaches the limit value

$$\xi_{m,\lim} = \frac{1}{1 + \sqrt[3]{\psi^2}} \sqrt{\frac{1+\psi^2}{2 - \sqrt[3]{\psi^2}}}, \tag{32}$$

the resonance peak vanishes and the modulus decreases monotonically, as in the case of real viscous damping models. As evinced in [6], this qualitative dynamic behaviour is similar in the range $-2\sqrt{2} < \psi < 0$.

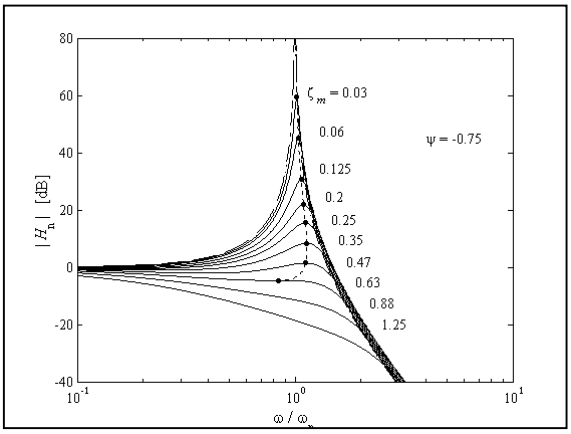

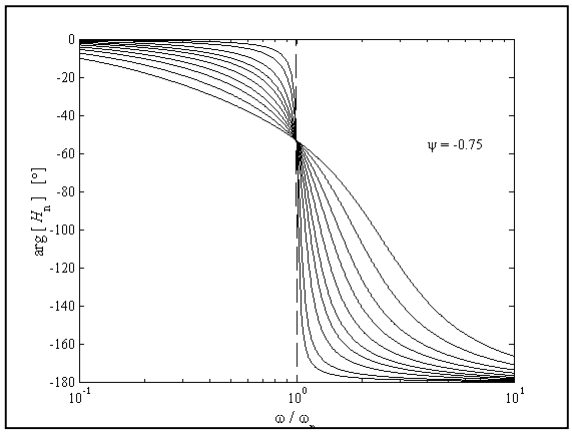

Fig. 10. and 11. Frequency response function modulus (up) and phase (down) with $\psi = -0.75$

4. CASE STUDY: EULER-BERNOULLI BEAM WITH PERMANENT MAGNETS

4.1 THEORETICAL MODEL

The analytical model is then applied to an uniform cantilever clamped-free Euler-Bernoulli beam in bending vibrations (thickness *h*, sizes *l* and *w* relative to *x*, *y* and *z* axes), whose dynamic behaviour is modified by the presence of a pair of concordant or discordant magnets settled at the free end.

With regards to the full coupling magneto-mechanical problems [14], in this model the magnetic effects are taken into account through a lumped translational complex viscous damping element at the free end of the beam. In fact, according to the theoretical model, the magnetic effects result strictly localised on the magnetic flux tube which corresponds to the projection of the magnets surfaces on the beam.

The partial differential equation of motion for an uniform Euler-Bernoulli beam with distributed viscous damping in bending vibrations is [15]

$$\rho A \frac{\partial^2}{\partial t^2} u(y,t) + \mathrm{C}_v \frac{\partial}{\partial t} u(y,t) + E I \frac{\partial^4}{\partial y^4} u(y,t) = f(y,t) \tag{33}$$

where ρA is the mass per length unit, ρ is the material density, A is the cross-section area, C_v is the viscous damping proportional coefficient per length unit, EI is the bending stiffness, E is Young's modulus of elasticity, I is the area moment of inertia, u is the bending displacement, y is the spatial variable and f is the external force density. The boundary conditions that must be satisfied at $y = 0$ (clamped end) and $y = l$ (free end) are:

$$\begin{cases} u(0,t) = 0 \\ \left[\dfrac{\partial}{\partial y} u(y,t)\right]_{y=0} = 0 \end{cases} \quad \text{and} \quad \begin{cases} \left[\dfrac{\partial^2}{\partial y^2} u(y,t)\right]_{y=l} = 0 \\ \left[\dfrac{\partial^3}{\partial y^3} u(y,t) - \mathrm{L}[u(y,t)]\right]_{y=l} = 0 \end{cases}, \tag{34}$$

where the linear differential operator L in the equilibrium equations depend on the lumped complex viscous damping element at $y = l$.
In absence of external forces, through the separation of variables $u(y,t) = \phi(y)\, q(t)$ the boundary-value problem of Eqs. (33) and (34) becomes a differential eigenvalue problem; hence the eigenfunctions $\phi(y)$ can be written as function of eigenvalues s in the form

$$\phi(y) = \gamma_1 e^{+\lambda y} + \gamma_2 e^{-\lambda y} + \gamma_3 e^{+\mathrm{j}\lambda y} + \gamma_4 e^{-\mathrm{j}\lambda y}, \quad \text{with} \quad \lambda = \sqrt[4]{-\frac{\rho A s^2 + \beta_1 s}{\beta_2 s + E I}} \tag{35}$$

where β_1, β_2 are proportionality coefficients; thus, the boundary conditions of Eq. (34) become

$$\begin{cases} \phi(0) = 0 \\ \phi'(0) = 0 \end{cases} \quad \text{and} \quad \begin{cases} \phi''(l) = 0 \\ \phi'''(l) - \dfrac{c_m - \mathrm{j}\, c_e}{E I} s\, \phi(l) = 0 \end{cases}; \tag{36}$$

hence the shear equilibrium condition depends on eigenvalues s.
The boundary conditions of Eq. (36) lead to the characteristic equation

$$\left[1 + \cosh(\lambda l)\cos(\lambda l)\right] + \frac{c_m - \mathrm{j}\, c_e}{\lambda^3\, E I} s \left[\cosh(\lambda l)\,\mathrm{sen}(\lambda l) - \mathrm{senh}(\lambda l)\cos(\lambda l)\right] = 0, \tag{37}$$

which can be solved numerically by using a secant method in the Argand-Gauss plane for the eigenvalues s. It is worth noting that if the external lumped translational damping element is removed, the damping results proportional; otherwise it becomes non-proportional, and consequently the eigenfunctions, or modal shapes, become complex: in general their phase is not constant with respect to the spatial variable y. In Fig. 12 and 13 the real and imaginary part of the first three complex eigenfunctions are shown in case of the experimental 3 mm thick aluminium beam, with an air gap Δ = 21 mm.

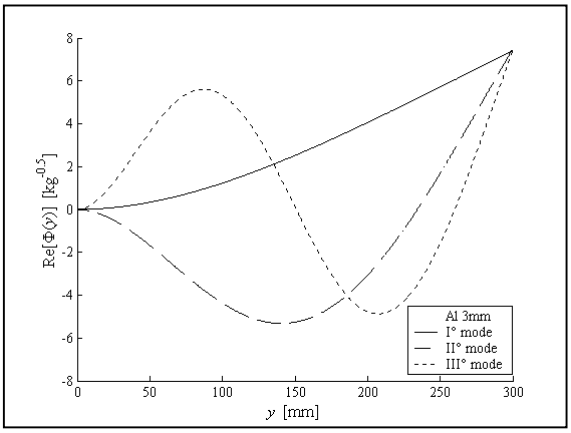

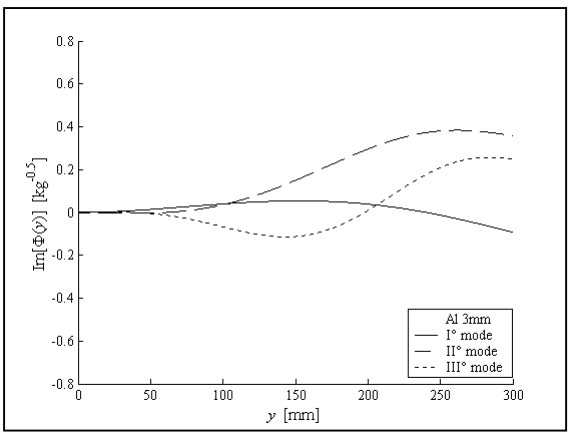

Fig. 12. and 13. Real (up) and imaginary (down) part of the first three complex eigenfunctions of the clamped-free beam with a lumped complex viscous damping element in $y = l$

If the beam is loaded at section $y = y_f$ with an external harmonic force $f(y,t) = f_0\ \delta(y - y_f)\,\mathrm{e}^{\mathrm{j}\,\omega\,t}$, where δ is the Dirac distribution, then the transfer function (receptance), evaluated in $y = y_o$, can be written as

$$\frac{u_0}{f_0}(y_f, y_o, \omega) = \sum_{n=1}^{\infty} \frac{\phi_n(y_f)\,\phi_n(y_o)}{-M_n\,\omega^2 + \mathrm{j}\,C_n\,\omega + K_n}, \tag{38}$$

where M_n, C_n and K_n are three complex modal parameters defined as

$$\begin{aligned} M_n &= \rho\,A \int_0^l \phi_n^2(y)\,d\,y \\ C_n &= \int_0^l \phi_n(y)\,\mathrm{C}_v[\phi_n(y)]\,d\,y \\ K_n &= E\,I \int_0^l \phi_n(y)\,\frac{d^4\,\phi_n(y)}{d\,y^4}\,d\,y = \lambda_n^4\,E\,I \int_0^l \phi_n^2(y)\,d\,y \end{aligned} \tag{39}$$

corresponding dimensionally to a modal mass, a modal damping and a modal stiffness, respectively.
If the eigenfunctions are normalised with respect to M_n, then the transfer function can be written in the form [15]

$$\frac{u_0}{f_0}(y_f, y_o, \omega) = \sum_{n=1}^{\infty} \frac{\hat{\phi}_n(y_f)\,\hat{\phi}_n(y_o)}{-\omega^2 + \mathrm{j}\,2\,\mathrm{Z}_n\,\Gamma_n\,\omega + \Gamma_n^2} \tag{40}$$

where Γ_n and Z_n are complex parameters corresponding dimensionally to a modal natural frequency and a modal damping factor, respectively. Note that if the damping is proportional, i.e. the external lumped damping element is removed, $\Gamma_n = \omega_n$ is the modal natural frequency and $\mathrm{Z}_n = \xi_n$ is the modal damping factor.

4.2 EXPERIMENTAL RESULTS AND CONCLUSIONS

In order to verify the theoretical model, a uniform cantilever clamped-free beam is considered (size l = 300 mm, w = 30 mm, thickness h = 2 or 3 mm), capable of satisfying the hypothesis of the Euler-Bernoulli beam (Fig. 14); a modal damping factor ξ_n = 0.001 is assumed to take into account the low structural damping of the beam.
Three kinds of materials have been tested: beams of aluminium (paramagnetic), copper and brass (diamagnetic), coupled with the two previously considered magnets, placed at the free-end of the beam in concordant or discordant configuration; the air gap Δ varies between 15 and 50 mm. In order not to modify the magneto-static field, the beam constraints and the structure holding the magnets are in aluminium.
Let the origin of the reference frame be set at the clamped end. Then, transfer functions due to a force acting at y_f = 45 mm have been experimentally determined in y_o = 215 mm, with

random or impulsive excitations in the frequency range 0-255 Hz; the resolution is 0.25 Hz and the mean value of 20 measures is considered.

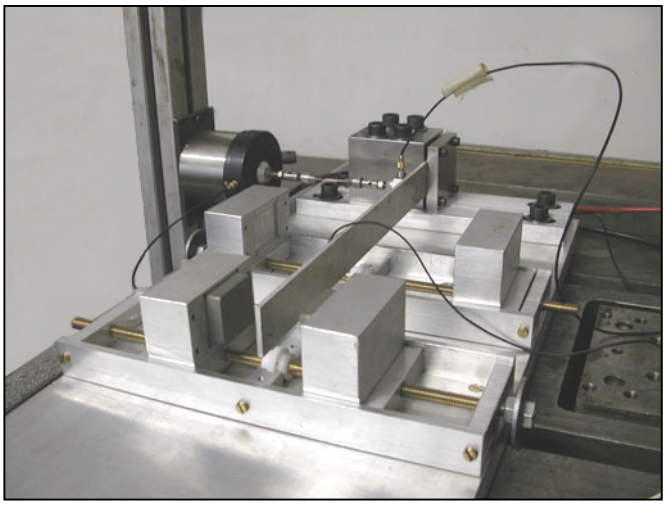

Fig. 14. Experimental set up

Experimental outcomes provide a complete validation of the theoretical magnetic and dynamic models: in fact, they are suitable to describe both the damping and the dynamic stiffening effects.
In order to identify the parameters of the analytical model, an accurate fitting procedure on the experimental transfer functions has been performed, by means of a least square methodology (Fig. 15).

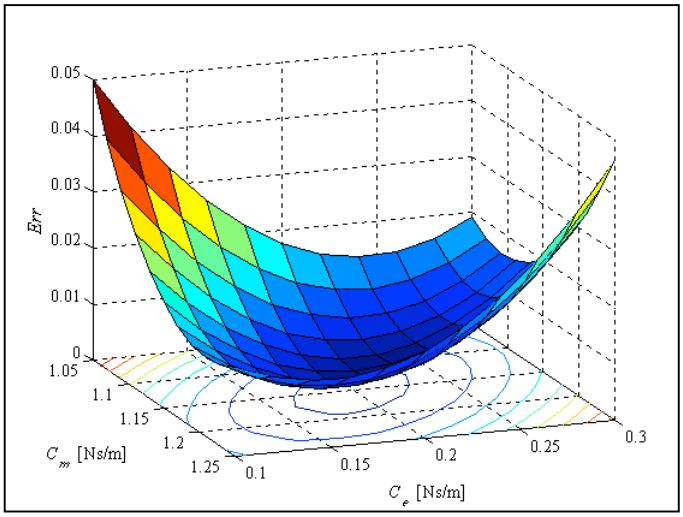

Fig. 15. LMS identification of the magnetic parameters

As shown in Fig. 16, significant differences in the damping property are evinced in concordant and discordant configurations.
In fact, by varying the air gap between the two magnets in concordant setup, the damping effect results very low. In accordance with experimental results, the magnetic model predicts a null distribution in the flux tube of the magnetic induction gradient in the undeformed configuration of the beam.
In discordant setup, the damping effect depends on the chosen air gap and it is very strong in materials with low electric resistivity, like aluminium (Fig. 18 and 20) and copper (Fig. 21), while it is relatively lower in brass (Fig. 17), characterised by a higher resistivity. The theoretical model perfectly predicts this behaviour.
Moreover, experimental data underline the dynamic effect of stiffening (depending on the acting force frequency) responsible for the shift of the resonance frequencies to higher values, as shown in Fig. 18, 20 and 21 for aluminium and copper beams, in complete accordance with the model predictions.
It is worth noting that, if the magnetic damping effect can not be tuned, the increase of stiffness in dynamic tests is difficult to appreciate. In particular the comparison between the beam without magnets and with a small air gap between the magnets demonstrates the effective dynamic stiffening.

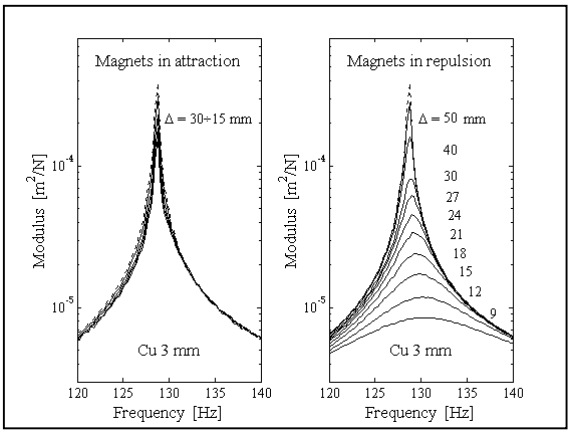

Fig. 16. Experimental magnetic effects on a copper beam

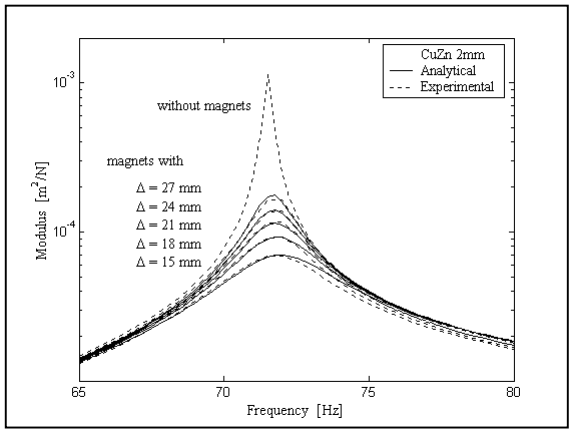

Fig. 17. Analytical-experimental transfer function modulus for a brass beam

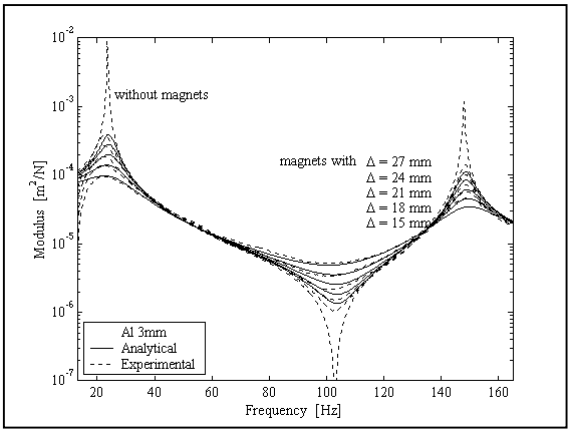

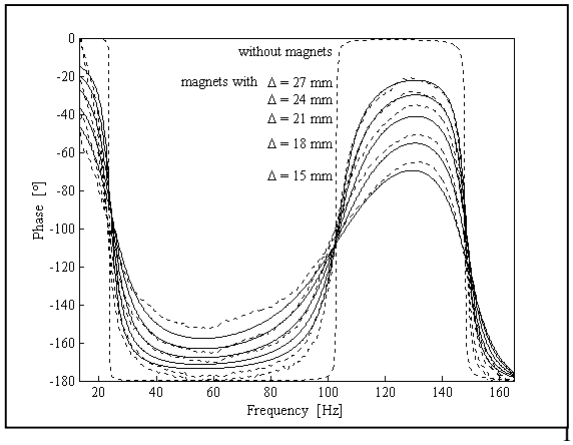

Fig. 18. Analytical-experimental transfer functions modulus for an aluminum beam

Fig. 19. Analytical-experimental transfer functions phase for an aluminum beam

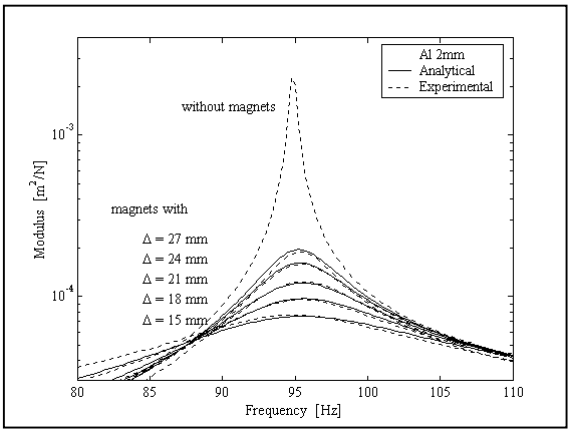

Fig. 20. Analytical-experimental transfer function modulus for an aluminum beam

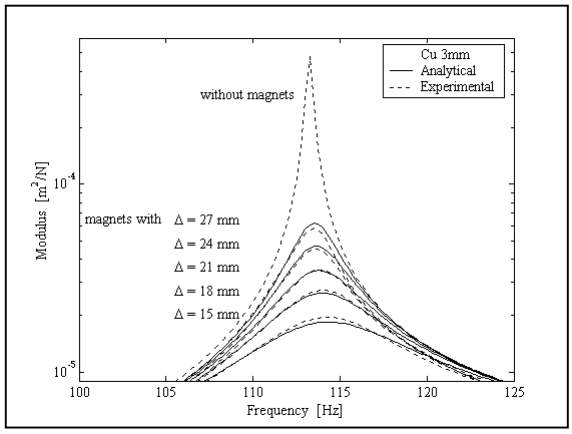

Fig. 21. Analytical-experimental transfer function modulus for a copper beam

The experimental values of c_m and c_e are in good accordance with those predicted through the theoretical magnetic model. Moreover, as shown in Table 1, the reliability of the complex viscous damping model (both in modulus and in phase) can be successfully validated by using a mean value of the magnetic induction gradient between the constant distribution of Eqs. (18) and (22) and the parabolic distribution of Eqs. (26) and (28).
According to the theoretical magnetic model, it is also possible to observe that coefficients c_m and c_e linearly depend on the thickness of the beam (Fig. 18 and 20).
Finally, it results that the ratio c_m / c_e is approximately constant (cfr. Fig 9) with respect to the air gap Δ under the hypothesis of a constant magnetic induction gradient distribution (Table 1).

Air gap Δ [mm]	Analytical model [Ns/m]				Experimental [Ns/m]	
	Constant		Parabolic			
	c_m	c_e	c_m	c_e	c_m	c_e
27	0.4984	0.1246	0.6639	0.1210	0.68	0.13
24	0.6810	0.1702	0.8786	0.1659	0.83	0.17
21	0.9458	0.2364	1.1659	0.2315	1.09	0.24
18	1.3412	0.3353	1.5548	0.3304	1.48	0.35
15	1.9551	0.4888	2.0930	0.4855	1.95	0.49

Table 1. Analytical-experimental parameters for a 3 mm thick aluminum beam

For a complete analysis of the experimental evinced stiffening magnetic effects, in analogy with the recent research of Zheng et al. [16], a different boundary condition problem has been investigated, by neglecting the phantom effect, i.e. c_e = 0, and modifying the

momentum boundary condition at the free end in order to take into account a viscous rotational damping term. Therefore the boundary condition of Eq. 35 may be replaced with

$$\begin{cases} \phi(0) = 0 \\ \phi'(0) = 0 \end{cases} \quad \text{and} \quad \begin{cases} \phi''(l) + \dfrac{c_m - \mathrm{j}\, c_e}{E\, I} b\, s\ \phi(l) = 0 \\ \phi'''(l) - \dfrac{c_m - \mathrm{j}\, c_e}{E\, I} s\ \phi(l) = 0 \end{cases} . \tag{41}$$

This choice, as shown in Fig. 22, is not able to justify the dynamic stiffening effect experimentally observed, whereas the phantom effect model is able to.

Experimental validation, hence, proves the reliability of the complex viscous damping model in describing both high damping and dynamic stiffening effects, due to eddy currents flowing into paramagnetic or diamagnetic materials with low electric resistivity.

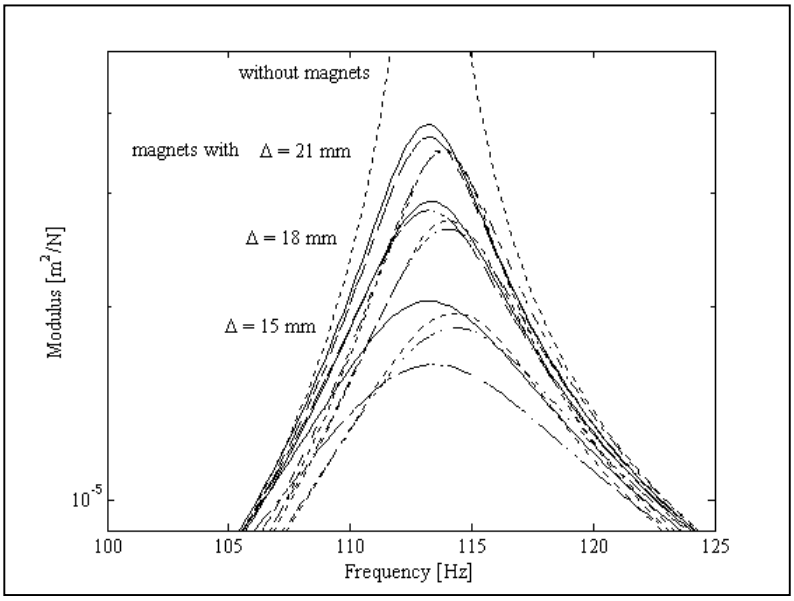

Fig. 22. Comparison in boundary conditions: (–) real viscous damping shear term, (--) real viscous damping shear and momentum terms, (–·) complex viscous damping shear term, (··) experimental transfer function

This paper is dedicated to the memory of Prof. Bruno A. D. Piombo, who unexpectedly died on November 2002, 26th, remembering his example and his participation to the university research.

REFERENCES

1. J.M.D. Coey, Permanent magnets applications. *Journal of Magnetism and Magnetic Materials* 248 (2002) 441-456.
2. J.P. Yonnet, Passive Magnetic Bearings with Permanent Magnets. *IEEE Transactions on Magnetics* 14 (1978) 803-805.
3. K. Nagaya, Y. Karube, A Rotary Magnetic Damper or Brake Consisting of a Number of Sector Magnets and a Circular Conductor. *ASME Journal of Dynamics Systems, Measurement, and Control* 111 (1989) 97-104.

4. F.C. Moon, *Magneto-Solid Mechanics*, John Wiley & Sons Inc., New York, 1984.
5. W. Yang, H. Pan, D. Zheng, Q. Cai, Vibration and dynamic instability of ferromagnetic thin plates in magnetic fields. *Mechanics Research Communications* 26(2) (1999) 239-244.
6. B.A.D. Piombo, E. Bonisoli, M. Ruzzene, A theoretical model of oscillations of paramagnetic or diamagnetic structures subject to passive magnetic elements, *Proceedings of DETC'01 ASME 2001*, Pittsburgh, Pennsylvania, September 2001.
7. H.S. Nagaraj, Investigation of Magnetic Fields and Forces Arising in Open-Circuit-Type Magnetic Bearings. *Tribology Transactions* 31 No. 2 (1988) 192-201.
8. W.F. Brown, *Magnetoelastic Interactions Tracts in Natural Philosophy*, Springer-Verlag, New York, 1966.
9. E. Bonisoli, A. Vigliani, Static behaviour of magneto-elastic forces, *16th AIMETA Congress of Theoretical and Applied Mechanics*, Ferrara, Italy, September 2003.
10. J. Guckenheimer, P. Holmes, *Nonlinear Oscillations, Dynamical Systems, and Bifurcations of Vector Fields*, Springer-Verlag, New York, 1990, 3 ed., pp.82-91.
11. K. Nagaya, H. Kojima, Y. Karube, H. Kibayashi, Braking Forces and Damping Coefficients of Eddy Current Brakes Consisting of Cylindrical Magnets and Plate Conductors of Arbitry Shape. *IEEE Transactions on Magnetics* 20 No. 6 (1984) 2136-2145.
12. S.H. Crandall, The role of damping in vibration theory. *Journal of Sound and Vibration* 11 (1970) 3-18.
13. L. Gaul, S. Bohlen, S. Kempfle, Transient and forced oscillations of systems with constant hysteretic damping. *Mechanics Research Communications* 12(4) (1985) 187-201.
14. T. Takagi, J. Tani, Dynamic behavior analysis of a plate in magnetic field by full coupling and MMD methods. *IEEE Transactions on Magnetics* 30 No. 5 (1994) 3296-3299.
15. L. Meirovitch, *Principles and techniques of vibrations*, Prentice-Hall International Inc., New York, 1997.
16. X.J. Zheng, Y. Zhou, K. Miya, An analysis of variable magnetic damping of a cantilever beam-plate with end coils in transverse magnetic fields. *Fusion Engineering and Design* 55 (2001) 457-465.